https://doi.org/10.1016/j.apcatb.2020.119548

Ni Nanoparticles on Active (001) Facet-Exposed Rutile TiO_2 Nanopyramid Arrays for Efficient Hydrogen Evolution

Yong Li,[a] Kyung-Ah Min,[b] Byungchan Han,[b,] and Lawrence Yoon Suk Lee[a,]**

Y. Li, Dr. K.-A. Min, Prof. B. Han, Dr. L. Y. S. Lee

[a] Department of Applied Biology and Chemical Technology and the State Key Laboratory of Chemical Biology and Drug Discovery, The Hong Kong Polytechnic University, Hung Hom, Kowloon, Hong Kong SAR

[b] Department of Chemical and Biomolecular Engineering, Yonsei University, Seoul, Republic of Korea.

* Corresponding authors:

E-mails: bchan@yonsei.ac.kr (B. Han); lawrence.ys.lee@polyu.edu.hk (L. Y. S. Lee)

Abstract

Efficient earth-abundant electrocatalysts for hydrogen evolution reaction (HER) is crucial for realizing cost-effective hydrogen production as a renewable energy source. Herein, we report highly enhanced HER activity of Ni nanoparticles (NPs) on TiO_2 nanopyramid arrays (NPAs). The (001) facets exposed on TiO_2 NPAs provide strong adsorption sites for Ni NPs, and the charge redistribution between Ni NPs and TiO_2 tunes the adsorption energy of HER intermediates, optimizing HER activity as manifested by low overpotential of 88 mV at 10 mA cm^{-2} and Tafel slope of 78 mV dec^{-1}. The modification of the Ni/TiO_2 NPAs with nitrogen-doped carbon quantum dot layer forms an active interface of Ni-N-C bonds, which enhances the stability and activates the Ni NPs on inactive {110} facets to further lower the overpotential to 65 mV at 10 mA cm^{-2}. This work provides a new insight into rational design of non-noble metal electrocatalysts for highly promoted hydrogen production.

Keywords: Ni nanoparticles; TiO_2 nanopyramid; facet engineering; hydrogen evolution reaction; electrocatalyst

Graphical Abstract

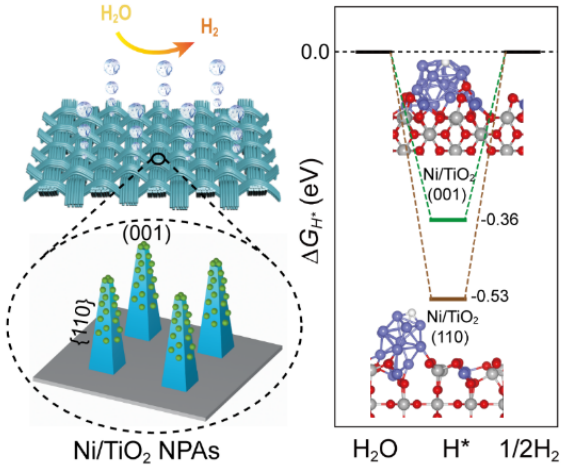

Thanks to the strong electronic interaction between Ni and the active (001) facet of TiO_2, Ni nanoparticles on TiO_2 nanopyramid arrays show an excellent hydrogen evolution activity with an overpotential of 88 mV at 10 mA cm^{-2} and a Tafel slope of 78 mV dec^{-1}, which is superior to Ni/TiO_2 nanowire arrays.

Highlights

- TiO_2 nanowire arrays (NWAs) and nanopyramid arrays (NPAs) were vertically grown on carbon cloth.
- F^- ions adjust the surface energy of TiO_2, exposing new (001) facets in addition to {110} facets in TiO_2 NPAs.
- The Ni nanoparticles deposited on TiO_2 NPAs show the HER activity superior to those on TiO_2 NWAs.
- The modification of TiO_2 NPAs with N doped C quantum dots further activated Ni nanoparticles by forming active Ni–N–C bonds.

1 Introduction

Hydrogen is an ideal next-generation energy carrier that can potentially resolve current energy and environmental issues caused by the excessive use of fossil fuels.[1,2] Among various technologies available, electrochemical water splitting, consisting of two half-reactions: oxygen evolution reaction (OER) and hydrogen evolution reaction (HER), is considered as the most promising pathway toward the renewable and eco-friendly hydrogen production for sustainable applications.[3,4] The more sluggish OER is usually catalyzed under alkaline conditions.[5] It is thus desirable to develop the HER catalysts that are highly active yet long-term stable under the same conditions. To date, Pt is known as the state-of-the-art HER catalyst because of the optimal hydrogen adsorption energy, but its wide application is largely limited by the high cost and scarcity.[6] Hence, searching for highly active and low-cost non-precious materials have attracted great interest. In recent years, transition metals (TMs), such as Ni, Fe, Co, and Mo, are extensively studied as potential HER catalysts. In particular, Ni received much attention owing to its crustal abundance, low price, good corrosion resistance, and similar Gibbs free energy of adsorbed H (ΔG_{H*}) intermediate to Pt.[7,8] However, the stronger binding energy to hydrogen than Pt poses the difficulty in removing the produced molecular hydrogen.[9,10] Besides, water dissociation which is the rate determining step for HER in alkaline solution is also inefficient on TMs surfaces, lowering the catalytic activity.[11] To improve their HER performance, metal oxides or sulfides are recommended to composite with TMs to form an optimal hybrid catalyst on the ground of following two advantages: 1) the surface electronic state of TMs can be adjusted by the strong electronic interactions between

TMs and metal compounds for efficient hydrogen adsorption and desorption; 2) those metal compounds are effective for cleaving H-OH bond, which can accelerate the water dissociation for HER.[12,13]

Titanium oxide (TiO_2) is a typical *n*-type semiconductor and has been widely used as a photo(electro)catalyst for solar water splitting and solar cells, especially single-crystal anatase and rutile TiO_2.[14,15] Due to low electronic conductivity, TiO_2 has been considered inefficient to be an active catalyst for HER, yet recent researches indicated that it can work as a promising support to optimize the HER performance of metallic catalysts in a TiO_2-TM system, for instance, TiO_2 nanodots/Co nanotubes,[13] MoS_2@TiO_2,[16] and $Ru_{0.33}Se$@TiO_2 nanotube arrays.[17] The majority of TiO_2-based HER catalysts, however, suffer from high overpotential that exceeds 150 mV to attain a current density of 10 mA cm^{-2} and often need further treatments for improvement. In photocatalysis, the reactivity of TiO_2 is known to be closely related to its surface chemistry.[18,19] For example, the {001} facets of anatase TiO_2 are more active than {101} facets, while anatase TiO_2 surfaces are normally dominated by the thermodynamically stable {101} facets.[20] To improve their photocatalytic activity, the surface of anatase TiO_2 was modified to have a high percentage of active (001) facets by reducing the surface energy of (001) facet to lower than that of {101} facets using F^- ions. A similar phenomenon has been also observed with rutile TiO_2.[21] However, it is still ambiguous whether the exposed facets of TiO_2 affect the electronic states of the TiO_2-TM system and their impact on HER.

With the advantages of high conductivity, low cost, and a large specific surface, carbon quantum dots (CQDs) have been widely explored as a supporting material in HER.[22–24] In

particular, CQDs-metal hybrid nanomaterials show better catalytic activity than other carbon-based materials (such as, graphene, C_{60}, or graphite).[25-27] Additionally, N dopants in carbon nanomaterials have been investigated as the heteroatom that can not only alter the electrical conductivity, basicity, and oxidation stability of carbon but also tune the work function of carbon to promote the catalytic activity of the hybrid nanomaterials.[28–30] Although nitrogen-doped carbon quantum dots (NC QDs) have been investigated and applied in some fields (*e.g.*, solar cell,[31] photocatalysis,[32] and fluorescence sensor[33]), the electrochemical HER activity of NC QDs-modified catalysts has been rarely reported.

In this work, we prepared novel TiO_2 nanopyramid arrays (NPAs) on carbon cloth by varying the concentration of F^- ions in the growth media, which expose additional (001) facets on the top surface compared to the conventional TiO_2 nanowire arrays (NWAs) that possess only the {110} surface. On TiO_2 NPAs and NWAs, Ni nanoparticles (NPs) are deposited by hydrothermal method in conjunction with a post-annealing process in 10 % H_2/N_2 atmosphere to investigate how the underlying TiO_2 nanostructure affect the HER activity of Ni. The intimate electronic interaction and hence the charge redistribution between Ni NPs and the highly active (001) facet of TiO_2 NPAs are supported by the X-ray photoelectron spectroscopy (XPS) data and density functional theory (DFT) calculations. Furthermore, we demonstrate that the construction of interface with NC QD layer further improves the catalytic HER activity and stability of Ni NPs on TiO_2 NPAs to deliver a low overpotential of 65 mV at 10 mA cm^{-2} and a small Tafel slope of 68.3 mV dec^{-1}.

2 Experimental section

2.1 Chemicals and Reagents

Carbon cloth (WOS1002) was purchased from CeTech Co., Ltd. Concentrated Hydrochloric acid (con. HCl), Hydrofluoric acid (con. HF), Nitric acid (con. HNO_3) were purchased from Duksan Pure Chemicals Co., Ltd. NH_4F were obtained from Sigma-Aldrich, Inc. Acetone and $Ni(NO_3)\cdot 6H_2O$ were purchased from Acros Organics, Thermo Fisher Scientific, Inc. Milli-Q water (15 MΩ cm, 25 ℃) was used to prepare solutions.

2.2 Synthesis of TiO_2 NPAs and NWAs

A piece of carbon cloth (2 cm × 3 cm) was washed in the following three solutions for 20 min each: 2 M HNO_3 (20 mL), ethanol (20 mL), and deionized water (DI-water, 20 mL). The cleaned carbon cloth was then immersed in a 0.5 M tetrabutyl titanate solution (TBT, 30 mL) for 40 min, followed by heating at 400 ℃ for 30 min in a muffle furnace to prepare TiO_2 seeds on carbon cloth. The TiO_2 seeds on carbon cloth was then put into a 100 mL Teflon-lined stainless autoclave containing 30 mL acetone, 30 mL concentrated HCl, 3 mL TBT, and 50 μL HF (2 M) and heated at 200 ℃ for 30 min. The autoclave was cooled down to room temperature, and the resulting TiO_2 NPAs were washed with DI water for three times and dried at room temperature overnight. The TiO_2 NWAs were prepared using the same procedure but without the HF solution in the growth solution.

2.3 Synthesis of Ni/TiO_2 NPAs and NWAs

The carbon cloth coated with as-prepared TiO_2 NPAs was cut into small pieces (0.5 cm × 2 cm)

and put into 20 mL Teflon-lined stainless autoclave containing 0.05 g $Ni(NO_3)_2 \cdot 6H_2O$ and 0.3g NH_4F dissolved in 15 mL DI water. The autoclave was sealed and maintained at 180 ℃ for 10 h. The precursor was washed by ultrasonication in DI water for 20 min and dried at room temperature before annealing in a tube furnace at 450 ℃ for 70 min in a 10 % H_2/N_2 atmosphere to yield the Ni nanoparticles decorated TiO_2 NPAs. The Ni/TiO_2 NWAs were prepared by the same process using as-prepared TiO_2 NWAs. The Ni/TiO_2 NPAs and NWAs were etched with 2 M HNO_3 to remove the Ni NPs to yield control samples of Ni doped TiO_2 NPAs and NWAs (e-TiO_2 NPAs and NWAs). Ni NPs/CC was also prepared with the same method using carbon cloth instead of TiO_2 NPAs or NWAs. Ni-doped TiO_2 (Ni-TiO_2) NPAs was synthesized under the same hydrothermal conditions but only with 0.05 g $Ni(NO_3)_2 \cdot 6H_2O$ in DI water.

2.4 Synthesis of NC/Ni/TiO_2 NPAs and NWAs

A small piece (0.5 × 2 cm^2) of carbon cloth with TiO_2 NPAs was put into 20 mL Teflon-lined stainless autoclave containing 0.025g PAM, 0.05 g $Ni(NO_3)_2 \cdot 6H_2O$, and 0.3g NH_4F dissolved in 15 mL DI water. The same synthetic procedure for Ni/TiO_2 NPAs was employed to prepare NC/Ni/TiO_2 NPAs. The NC/Ni/TiO_2 NWAs and NC/Ni NPs/CC were also fabricated in the same way.

2.5 Characterizations

The morphology and structure of the samples were characterized by using a transmission electron microscope (TEM, Jeol JEM-2100F), scanning electron microscope (FESEM, TESCAN MAIA3), Raman spectroscope (Renishaw Micro-Raman), and X-ray diffractometer

(XRD, Rigaku SmartLab 9kW). The catalyst loading mass on carbon cloth was detected by inductively coupled plasma optical emission spectrometry (ICP-OES, Agilent 710). The chemical states of the samples were estimated by X-ray photoelectron spectroscopy (XPS, Thermo Fisher Scientific K-Alpha).

2.6 HER measurements

A three-electrode system was employed in 1 M KOH electrolyte to test all the electrochemical properties by CH Instrument (CHI760E, Cheng Hua, Shanghai). The as-prepared samples were directly used as the working electrode with an active surface area of 0.4 cm^2. A graphite rod and Hg/HgO electrode were used as the counter and reference electrode, respectively. All the potentials in this work were converted to the potentials *versus* the reversible hydrogen electrode (RHE) using the equation, $E_{RHE} = E_{Hg/HgO} + 0.098 + 0.059 \times pH$. Cyclic voltammetry (CV) was initially conducted within a potential range from 0.224 to -0.276 V at a scan rate of 50 mV s^{-1} in order to stabilize the electrodes prior to the evaluation of HER performance. For linear sweep voltammetric (LSV) measurements, the scan rate was set to 1 mV s^{-1}. All the LSV results in this work were calibrated by *i*R compensation (98 %). Electrochemical impedance spectroscopy (EIS) was performed at the potential of -1.15 V (*vs*. Hg/HgO reference electrode) and the scanning frequency values ranging from 100kHz to 0.05 Hz. The EIS results were fitted by a simplified Randles equivalent circuit. The detail calculation of the turnover frequency (TOF) was described in supporting information. The stability was estimated by an amperometric test at selected potentials.

2.7 First-principles calculations

We carried out first-principles density functional theory (DFT) calculations with electronic spin polarization to elucidate the underlying mechanism of the HER catalysis on different facets in Ni/TiO_2 materials. The calculations were performed within a generalized gradient approximation (GGA) for the exchange-correlation (*xc*) functionals,[34,35] implemented in the Vienna *ab-initio* simulation package (VASP).[36,37] The projector augmented wave (PAW) potentials were utilized to describe the electron-ion interaction.[38] The kinetic energy cut-off for the plane-wave basis was set to 400 eV. The Grimme's DFT-D3 method based on a semi-empirical GGA-type theory was adopted for the van der Waals (vdW) correction.[39] For a slab model, we used (4 × 2) and (3 × 3) unit cells of rutile TiO_2(110) and (001) surfaces, respectively. In the Ni/TiO_2 models, Ni atoms were substitutionally doped instead of the surface Ti atoms in TiO_2 and surface O defects were considered due to charge imbalance. Then, icosahedral Ni cluster consisting of 13 Ni atoms was adsorbed on the Ni-doped TiO_2 surfaces. For the Brillouin-zone integration in the reciprocal space, grid meshes of (2 × 2 × 1) were utilized with the Gamma-centered scheme. In the calculations, all models were fully relaxed to get equilibrium structures with the Hellmann-Feynman forces and energy convergence criteria of 0.05 eV $Å^{-1}$ and 1 × 10^{-5} eV, respectively.

We defined the binding energy (E_b) of Ni NPs and TiO_2 as Eq. (1)

$$E_b = E_{Ni/TiO_2} - E_{Ni} - E_{TiO_2} \quad (1)$$

where E_{Ni/TiO_2}, E_{Ni}, and E_{TiO_2} are the total energies of Ni/TiO_2, Ni NPs, and TiO_2, obtained

by DFT calculations, respectively. The plane-averaged charge density difference (Δn) was obtained by Eq. (2)

$$\Delta n = n_{Ni/TiO_2} - n_{Ni} - n_{TiO_2} \quad (2)$$

Here, n_{Ni/TiO_2}, n_{Ni}, and n_{TiO_2} mean the plane-averaged charge densities of Ni/TiO_2, Ni NPs, and TiO_2, respectively. The adsorption energy of H ($E_{H\text{-}ads}$) on Ni/TiO_2 was defined as Eq. (3)

$$E_{H-ads} = E_{H/Ni/TiO_2} - E_{Ni/TiO_2} - \frac{1}{2}E_{H_2} \quad (3)$$

where $E_{H/Ni/TiO_2}$, E_{Ni/TiO_2}, and E_{H_2} are total energies of Ni/TiO_2 with and without adsorbed H and a H_2 gas molecule, respectively. Gibbs free energy for H adsorption (ΔG_{H^*}) was evaluated by Eq. (4)

$$\Delta G_{H^*} = E_{H-ads} + \Delta E_{ZPE} - T\Delta S \quad (4)$$

Here, ΔE_{ZPE} and ΔS are the zero-point energy correction and entropy change due to H adsorption as defined in Eq. (5) and (6), respectively.

$$\Delta E_{ZPE} = E_{ZPE}(H^*) - \frac{1}{2}E_{ZPE}(H_2) \quad (5)$$

$$\Delta S = S(H^*) - \frac{1}{2}S(H_2) \approx -\frac{1}{2}S(H_2) \quad (6)$$

Then, the TΔS was estimated as -0.20 eV at 298 K and 1 bar with the entropy of gaseous H_2 in standard states.

3 Results and discussion

3.1 Characterization of TiO_2 NPAs and TiO_2 NWAs

The TiO_2 nanowires arrays (NWAs) and nanopyramid arrays (NPAs) were synthesized *via* a

two-step seed growth method as illustrated in **Fig. 1a**. In the first step, TiO_2 seeds are nucleated on the surface of carbon cloth, which are further grown to TiO_2 NWAs and NPAs in the subsequent hydrothermal reaction at 200 ℃ for 30 min. The morphology of TiO_2 NWAs and NPAs are characterized by scanning electron microscopy (SEM) and transmission electron microscopy (TEM). As shown in **Fig. 1b** and **1c**, the surface of carbon cloth is fully covered with the needle-like TiO_2 NWAs with an average width of 10 nm and length of 2 μm. Notably, the cross-sectional image (the inset in **Fig. 1b**) reveals a 2 μm thick TiO_2 layer formed as a base for TiO_2 NWAs. From the high-resolution TEM (HRTEM) image of TiO_2 NWAs (**Fig. 1d**), two well-defined lattice spacings of 0.32 and 0.29 nm are evident, which are assigned to the crystal planes of rutile TiO_2 (110) and (001), respectively, suggesting that the TiO_2 NWAs grow along the [001] axis and the exposed sidewalls are {110} facets. The growth mechanism of such TiO_2 NWAs can be described as follows: First, Ti atom bonds with six O atoms, forming the TiO_6 octahedrons as a growth unit. The neighbour TiO_6 octahedrons share a pair of opposite edges along the [001] direction to form a chain-like structure.[40] Kumar *et al*. confirmed that the growth rate of crystal faces in rutile TiO_2 NWAs follows the sequence of (110) < (100) < (101) < (001) because the available number of corners and edges of the coordination polyhedral varies.[41] As a result, the rutile TiO_2 NWAs is usually dominated by {110} facets.

Interestingly, the same seed-mediated growth procedure in the presence of 1.5 mM F^- ions results in a distinct pyramidal morphology of TiO_2. **Fig. 1e** shows the TiO_2 NPAs of an average length of *ca*. 3 μm, which are also vertically grown on the carbon cloth surface. The side-view SEM image (the bottom-left inset in **Fig. 1e**) clearly shows that each nanostructure consists of

four isosceles trapezoidal sidewalls with a flat top surface. The F^- ions apparently induced the growth of TiO_2 not only perpendicular to the [001] axis but also along the [001] axis, resulting in pyramidal morphology. **Fig. 1f** shows that the widths of the NPAs measure *ca*. 200 and 600 nm at the top and bottom region, respectively. Different from the NWAs, these TiO_2 NPAs are in direct contact with the carbon cloth as shown in the cross-sectional image (the top-right inset in **Fig. 1e**), suggesting that the F^- ions also prohibits the formation of thick TiO_2 layer. The single-crystalline nature of TiO_2 NPAs is supported by clear lattice fringes from the HRTEM images of top surface and sidewall (**Fig. 1g** and **h**, respectively) and the corresponding selected area electron diffraction (SAED) pattern (**Fig. 1i**). The lattice spacings of the TiO_2 NPAs are identical to those observed in the NWAs, indicating the same rutile phase. A close inspection of HRTEM images reveals the {110} and (001) facets from the sidewalls and top surface of TiO_2 NPAs, respectively. The rutile TiO_2 phase is also confirmed by the X-ray diffraction (XRD) patterns of TiO_2 NPAs and NWAs given in **Fig. S1**, ESI†, where the similar diffraction peaks observed at 27.4, 36.1, 41.2, and 54.3° are assigned to (110), (101), (111), and (211) plane of rutile TiO_2 phase, respectively (JCPDS 21-1276).[42] Notably, when the TiO_2 NWAs and NPAs are scratched off the carbon cloth, the (110) diffraction peak gets much intensified compared to the others, indicating that the surfaces of NWAs and NPAs are predominated by {110} facets (**Fig. S2**). We also compared the surface area of two nanostructures using the Brunauer-Emmett-Teller (BET) analysis as shown in **Fig. S3**. The TiO_2 NWAs obviously show a larger specific surface area of 73 $m^2\ g^{-1}$ than NPAs (65 $m^2\ g^{-1}$), benefiting from the high density of thinner nanowires.

3.2 Characterization of Ni/TiO_2 NPAs and Ni/TiO_2 NWAs

We then deposited Ni nanoparticles (NPs) onto these as-synthesized TiO_2 nanostructures (denoted as Ni/TiO_2 NPAs and NWAs, respectively) by a hydrothermal reaction at 180 °C to investigate how the underlying TiO_2 nanostructures affect the catalytic HER performance. The SEM images in **Fig. 2a** and **2b** confirm that both TiO_2 NWAs and NPAs retain their morphologies during the Ni NP deposition. The corresponding TEM images (the insets in **Fig. 2a** and **2b**) clearly show the Ni NPs (average d = *ca*. 20 nm). In the case of Ni/TiO_2 NWAs, the Ni NPs are only deposited on the {110} facets, whereas they are evenly distributed on both (001) and {110} facets of Ni/TiO_2 NPAs. The HRTEM images in **Fig. 2c** and **2d** reveal the well-defined fringes of Ni NPs with a lattice spacing of 0.203 nm, corresponding to the (111) planes of the metallic Ni phase. The hydrothermal deposition process of Ni NPs may also induce the Ni doping on TiO_2 surface. We prepared two control samples by etching the Ni NPs from Ni/TiO_2 NPAs and NWAs in 1.0 M HNO_3, which are denoted as e-TiO_2 NPAs and NWAs, respectively. The TEM images in **Fig. S4** confirm that the Ni NPs are completely removed from both TiO_2 NPAs and NWAs. The XRD patterns of Ni/TiO_2 NPAs and NWAs in **Fig. 2e** show two sets of diffraction peaks which are indexed to rutile TiO_2 and metallic Ni phases (JCPDS 04-0850), respectively. In contrast, only rutile TiO_2 peaks are observed in the XRD patterns of e-TiO_2 NPAs and NWAs, confirming the removal of Ni NPs. However, element mapping images reveal the uniform distribution of Ni, Ti, and O elements in the etched samples (**Fig. S4**), which indicate that some of Ti^{4+} ions in TiO_2 NPAs and NWAs were substituted by Ni^{2+} ions during hydrothermal reaction, owing to the similar ionic radius between Ni^{2+} (0.72 Å) and

Ti^{4+} (0.68 Å).[43] **Fig. 2f** compares the loading masses of Ni NPs and doped Ni estimated by inductively coupled plasma optical emission spectrometry (ICP-OES). The Ni/TiO_2 NWAs contains *ca*. 0.83 mg cm^{-2} Ni NPs, slightly higher than Ni/TiO_2 NPAs (0.65 mg cm^{-2}). This can be attributed to the larger surface area of TiO_2 NWAs (73 m^2 g^{-1}) than TiO_2 NPAs (65 m^2 g^{-1}) which provides more sites available for Ni NP deposition. Meanwhile, the e-TiO_2 NPAs and NWAs are doped with 0.07 and 0.08 mg cm^{-2} Ni, respectively, which account *ca*. 1.2 wt% of TiO_2 (**Fig. 2f** and **S5**). The loading amount of Ni NPs is nearly 10 times of the doped Ni, indicating that it would play a major role in the HER catalysis.

The composition and chemical states of these as-prepared Ni/TiO_2 NPAs, Ni/TiO_2 NWAs, e-TiO_2 NPAs, and e-TiO_2 NWAs were compared by X-ray photoelectron spectroscopy (XPS). The XPS spectra were first calibrated by adjusting the binding energy of C-C peaks to 284.8 eV in C 1s spectra (**Fig. S6a**).[44] The Ni $2p_{3/2}$ spectrum of Ni/TiO_2 NPAs displays three peaks located at 852.2, 855.7, and 860.9 eV, assigned to Ni^0, Ni^{2+}, and satellite peaks, respectively (**Fig. 3a**).[45] In particular, a noticeable Ni^{2+} peak shift of 0.3 eV compared to that of e-TiO_2 NPAs (855.4 eV). The Ni $2p_{3/2}$ spectrum of Ni/TiO_2 NWAs also displays three peaks at 852.2 (Ni^0), 855.7 (Ni^{2+}), and 861.2 eV (satellite). However, the binding energy of Ni^{2+} peak is unchanged from e-TiO_2 NWAs. The high resolution O 1s spectra of all samples (**Fig. 3b**) have two peaks that are assigned to the lattice oxygen (Metal-O bonds) at lower binding energies and hydroxyl group on surface (-OH) at higher binding energies.[46] Besides, additional peaks for adsorbed H_2O (H_2O_{ad}) appear in Ni/TiO_2 NPAs and NWAs, indicating that Ni NPs are beneficial for H_2O adsorption, an important step for HER in alkaline condition.[11] It is worth

to note that the M-O peak of Ni/TiO_2 NPAs (529.9 eV) also shows a positive shift of 0.5 eV from that of e-TiO_2 NPAs (529.4 eV), whereas the M-O peak occurs at the same binding energy (529.7 eV) in both Ni/TiO_2 and e-TiO_2 NWAs. Similarly, the high resolution Ti 2p spectra in **Fig. S6b** also show a discernible shift of Ti 2p peak only in the case of Ni/TiO_2 NPAs. These binding energy shifts in Ni^{2+}, M-O, and Ti^{4+} species in Ni/TiO_2 NPAs imply that there is a strong coupling effect between Ni NPs and TiO_2 NPAs owing to the existence of (001) surface, and thus the electronic states of Ni NPs on (001) facet would be tuned by such strong electronic interactions with TiO_2, which is absent for those on {110} facets.

3.3 Theoretical study of Ni/TiO_2 structure

We then compared the electronic interactions of Ni NPs with rutile TiO_2(110) and TiO_2(001) by first-principles density functional theory (DFT) calculations to validate the experimental observations. Our calculations show that Ni NP is strongly adsorbed on TiO_2(001) with binding energy (E_b) of -64.5 meV $Å^{-2}$, compared to the adsorption on TiO_2(110) which has E_b of -56.2 meV $Å^{-2}$. Such different binding strength of Ni NPs by supported TiO_2 facets affects the charge distribution at Ni NPs and TiO_2 interfaces. Using Eq. (2) in the experimental details, we obtained the plane-averaged charge density difference (Δn) of Ni/TiO_2(110) and (001) in **Fig. 3c** and **3d**, respectively. The Δn indicates the change of charge distribution (especially at Ni/TiO_2 interfaces) induced by interaction between Ni NPs and TiO_2. Here, the charge accumulation and depletion regions are marked with yellow and navy colours, respectively. The Δn indicates that charge depletion and accumulation dominantly appeared in Ni NP and TiO_2 (especially surface O atoms), respectively, regardless of TiO_2 facets; it means

the charge transfer from Ni NP to TiO_2 and electron deficiency in Ni NP. However, the amount of charge transfer is different depending on the binding strength between Ni NP and TiO_2. In this connection, the variation in number of charges was quantitatively examined by integrating the Δn in the vicinity of Ni NP and surface O atoms in TiO_2. For the Ni/TiO_2(110), we show that Ni NP is positively charged with electron loss about 0.48*e*, while surface O atom in TiO_2(110) is negatively charged with electron gain about 0.28*e*. However, more charge variation appears in Ni/TiO_2(001) with electron loss of 0.54*e* in Ni NP and electron gain of 0.51*e* in surface O atoms in TiO_2(001). Such different amounts of charge distribution by supported TiO_2 facets influence the adsorption energies of H ($E_{H\text{-}ads}$) on Ni NPs.

3.4 HER activities of Ni/TiO_2 NPAs and Ni/TiO_2 NWAs

The electronic coupling of Ni NP with the underlying TiO_2 facets was evaluated by investigating the HER activities of the samples using a standard three-electrode system in 1.0 M KOH. **Fig. 4a** compares the linear sweep voltammograms (LSV), where the Ni/TiO_2 NPAs exhibit an excellent HER performance with a low overpotential of 88 mV to deliver a current density of 10 mA cm^{-2}. The negligible HER activity of carbon cloth substrate (483 mV at 10 mA cm^{-2}) assures that the catalytic activity of as-prepared samples stems from the materials grown on it. The e-TiO_2 NPAs show a much higher overpotential of 418 mV to reach 10 mA cm^{-2}. The etching process would remove the Ni^{2+} on TiO_2 surface, which might be active for HER. To verify this, TiO_2 NPAs were directly doped with Ni (Ni-TiO_2 NPAs) and the HER activity was compared with e-TiO_2. As shown in **Fig. S7**, the polarization curve of Ni-TiO_2 NPAs is nearly overlapping that of e-TiO_2, indicating the surficial Ni^{2+} species does not

improve the HER activity much. On the other hand, the Ni NPs prepared on CC (Ni NPs/CC) demonstrates an overpotential of 285 mV at 10 mA cm^{-2}, suggesting the higher HER activity of Ni NPs than that of doped Ni atoms. Despite the higher loading of Ni NPs than in Ni/TiO_2 NPAs, Ni/TiO_2 NWAs exhibit only slightly enhanced overpotential of 286 mV at 10 mA cm^{-2}, which is not much different from e-TiO_2 NWAs (395 mV at 10 mA cm^{-2}), suggesting that the Ni NPs deposited on {110} facets afford a low HER activity. The remarkable HER enhancement of Ni/TiO_2 NPAs can be thus correlated to the Ni NPs on the highly active (001) facet of TiO_2 NPAs. The Tafel slope determined by fitting the linear part of Tafel plot provides useful kinetic information (**Fig. 4b**). The Ni/TiO_2 NPAs shows the lowest Tafel slope of 78 mV dec^{-1}, followed by e-TiO_2 NPAs, e-TiO_2 NWAs, and Ni/TiO_2 NWAs (146, 280, and 300 mV dec^{-1}, respectively). Such Tafel slope of Ni/TiO_2 NPAs implies that the HER on Ni/TiO_2 NPAs follows a two-electron transfer process with Volmer-Heyrovsky mechanism. In the amperometric *i*-t test at an overpotential of -126 mV engaged to evaluate the stability of Ni/TiO_2 NPAs (**Fig. 4c**), only *ca*. 82 % of current density was maintained after 17 h, disclosing the rather unstable nature of Ni/TiO_2 NPAs.

The number of active sites can largely affect the catalytic performance. We thus estimated the electrochemical surface areas (ECSAs) of samples by calculating the double layer capacitance (C_{dl}) from a series of cyclic voltammograms (CV) as shown in **Fig. 4d** and **S8**.[47] The C_{dl} of e-TiO_2 NWAs is merely 1.4 mF cm^{-2}, which slightly increases to 2.3 mF cm^{-2} with the deposition of Ni NPs. On the other hand, the C_{dl} of Ni/TiO_2 NPAs reaches 8 mF cm^{-2}, which is about 2.6 times larger than e-TiO_2 NPAs, confirming that the Ni NPs on TiO_2(001) facets

provide more electrochemically accessible sites than those on the {110} facets. The electrochemical impedance spectroscopy (EIS) was employed to investigate the reaction kinetics. From the Nyquist plots in **Fig. S9**, Ni/TiO_2 NPAs exhibit the smallest charge transfer resistance (R_{ct}) of 9 Ω in comparison with Ni/TiO_2 NWAs (47 Ω), e-TiO_2 NWAs (82 Ω), e-TiO_2 NPAs (296 Ω), and carbon cloth (555 Ω), indicating the favorable charge transfer kinetics of Ni/TiO_2 NPAs. The turnover frequency (TOF), obtained at an applied potential of 300 mV, was used to further compare the intrinsic activity of active sites on Ni/TiO_2 NPAs and NWAs. With the TOF of 0.24 s^{-1}, Ni/TiO_2 NPAs show the higher catalytic activity than Ni/TiO_2 NWAs (0.14 s^{-1}), in good agreements with electrochemical observations (**Fig. 4e**). To gain deeper insights on the difference in HER activity, the H adsorption on Ni/TiO_2(110) and (001) were investigated by first principles DFT calculations. The atomic configurations of H adsorbed Ni/TiO_2(110) and (001), represented in **Fig. S10**, show that H thermodynamically prefers to adsorb on fcc sites of both Ni NPs deposited on TiO_2(110) and (001). However, H weakly adsorbs on Ni/TiO_2(001) with $E_{H\text{-}ads}$ of -0.59 eV compared to Ni/TiO_2(110) with $E_{H\text{-}ads}$ of -0.75 eV. It is attributed to the dissimilar electron deficiency in Ni NP depending on the TiO_2 facets; the more electron deficiency in Ni NP, the weaker interaction with H. Furthermore, dissimilar $E_{H\text{-}ads}$ on Ni/TiO_2(110) and (001) induces the different Gibbs free energy (ΔG_{H^*}) for the H adsorption. As shown in **Fig. 4f**, we calculated the ΔG_{H^*} of -0.53 and -0.36 eV on the Ni/TiO_2(110) and (001), respectively. It indicates that both adsorption and desorption of H are more feasible on Ni/TiO_2(001) which has ΔG_{H^*} closer to 0 eV with reduced $E_{H\text{-}ads}$, as proposed by the Sabatier principle.[48] Thus, the improved HER performance is obtained on the Ni/TiO_2

NPAs that possess the (001) facets.

3.5 NC QDs modification on Ni/TiO_2 NPAs and Ni/TiO_2 NWAs

Considering the geometric structure of TiO_2 NPAs (**Fig. 1f**) in which the exposed surface area of {110} facet is almost 120 times of (001) facet, the HER activity of Ni/TiO_2 NPAs is believed to arise mainly from the small portion of optimized Ni NPs on (001) facets while a considerable amount of Ni NPs on {110} facets conveys a poor HER activity. Aiming to further improve the HER activity as well as the stability of the Ni/TiO_2 NPAs, we activated these Ni NPs on {110} facets by engaging polyacrylamide (PAM) during the hydrothermal synthesis of Ni NPs and incorporated a layer of nitrogen-doped carbon quantum dots (NC QDs) onto the Ni/TiO_2 NPAs (NC/Ni/TiO_2 NPAs).[49,50] The SEM and TEM analyses of obtained NC/Ni/TiO_2 NPAs, given in **Fig. S11**, reveal that the Ni/TiO_2 NPAs are covered with a thin (*ca*. 3 nm) layer containing numerous tiny carbon QDs (average d = *ca*. 2.5 nm). The uniform distribution of Ni, Ti, N, C, and O elements has been confirmed with the element mapping images by energy-dispersive X-ray spectra (EDX, **Fig. S12**). To compare the effect of NC QD layer, the Ni/TiO_2 NWAs were also treated in the same way to yield NC/Ni/TiO_2 NWAs as a control sample. Similar thin NC QD layer on the Ni/TiO_2 NWAs is evident from the TEM images in **Fig. S13**. In addition, the characteristic N-C peaks observed in C 1s and N 1s XPS spectra of NC/Ni/TiO_2 NPAs and NWAs (**Fig. S14** and **S15**) further confirm the nitrogen doping in carbon QD layer. Note the positive shifts of characteristic Ni^0, Ni^{2+}, M-O, and Ti^{4+} peaks upon the incorporation of NC QD layer on Ni/TiO_2 NPAs. Such peak shifts are absent in the case of NC/Ni/TiO_2 NWAs, implying that the underlying TiO_2 substrate still plays an important role in influencing the

electronic state of Ni.

The HER activities of as-prepared NC/Ni/TiO_2 NPAs and NWAs are compared with Ni/TiO_2 NPAs and NWAs in **Fig. 5a**. At a current density of 10 mA cm^{-2}, the NC/Ni/TiO_2 NPAs record the lowest overpotential of 65 mV, improved from 88 mV of Ni/TiO_2 NPAs. Interestingly, the incorporation of NC QD layer has even more profound effect on the Ni/TiO_2 NWAs, of which overpotential at 10 mA cm^{-2} drops from 286 to 104 mV (NC/Ni/TiO_2 NWAs). The corresponding Tafel slopes display a similar trend (**Fig. 5b**) where NC/Ni/TiO_2 NPAs mark the smallest (68.3 mV dec^{-1}), followed by Ni/TiO_2 NPAs (78.0 mV dec^{-1}), NC/Ni/TiO_2 NWAs (84.5 mV dec^{-1}), and Ni/TiO_2 NWAs (300.0 mV dec^{-1}). The NC/Ni/TiO_2 NWAs again show the greater enhancement than NC/Ni/TiO_2 NPAs, as summarized in **Fig. 5c** and **5d**. These remarkable enhancements in HER activity clearly indicate a positive coupling effect that creates an active interface between NC QD and Ni NP. Especially, the previously inactive Ni NPs on {110} facets are now activated, which explains the greater impact on Ni/TiO_2 NWAs. The Nyquist plots show that the charge transfer resistances (R_{ct}) of NC/Ni/TiO_2 NWAs and NPAs are reduced to 11 and 6 Ω from 47 and 9 Ω of Ni/TiO_2 NWAs and NPAs, respectively (**Fig. S16a**), indicating more favorable kinetics with NC QD layer. In addition, the ECSAs of NC/Ni/TiO_2 NPAs and NWAs were estimated by calculating the C_{dl} values (**Fig. S16b**). The C_{dl} of NC/Ni/TiO_2 NWAs has increased to 2.9 mF cm^{-2} compared with Ni/TiO_2 NWAs (2.3 mF cm^{-2}), implying the increased number of active sites in NC/Ni/TiO_2 NWAs. For the case of NC/Ni/TiO_2 NPAs, the C_{dl} has decreased from 8.4 to7.7 mF cm^{-2} upon the coating of NC QD layer. This suggests that the improved HER activity of NC/Ni/TiO_2 NPAs is due to the higher

intrinsic activity of Ni-N-C sties than Ni-Ni sites, not the number of active sites. For such high HER activity, the underlying TiO_2 NPAs are also important. Another control sample, NC/Ni NPs deposited on CC (NC/Ni NPs/CC), shows a poor HER performances with an overpotential of 245 mV at 10 mA cm^{-2} and Tafel slope of 121 mV dec^{-1} (**Fig. S17**), indicating the crucial role of TiO_2 NPAs for HER activity. The as-synthesized NC/Ni/TiO_2 NPAs exhibits a superior HER activity in comparison with most recently reported state-of-the-art Earth-abundant HER electrocatalysts (**Table S1**). The electrochemical stability of NC/Ni/TiO_2 NPAs also shows a remarkable enhancement. A stable current density is maintained with minimal loss of 6 % at applied potentials of -226 and -326 mV for continuous 30 h (**Fig. 5e**). **Fig. S18** also shows that the structure and morphology of NC/Ni/TiO_2 NPAs are will retained after HER test.

3.6 Active sites investigation of NC/Ni/TiO_2 NPAs and NC/Ni/TiO_2 NWAs

To obtain an insight into the HER mechanism at the active NC QDs/Ni NPs interface, *in situ* Raman spectroscopy was employed to investigate the reaction intermediates and the active sites for HER. At the applied potentials below -0.224 V, only two peaks are visible at 450 and 574 cm^{-1}, which are assigned to rutile TiO_2 vibration peaks (**Fig. 6a**). With the potential decreased to -0.274 V, a new broad peak appears at 820 cm^{-1}, which intensifies with the applied potential. This peak, assigned to the Ni-H vibrational band,[51] reveals the intermediate species still adsorbed on the Ni sites for subsequent H_2 generation and desorption. To further identify the active sites of NC/Ni/TiO_2 NPAs and NWAs, 5 mM potassium thiocyanate (KSCN) was added to 1.0 M KOH electrolyte during the amperometric *i*-t test. According to previous work,[52] SCN^- strongly adsorbs on Ni-N_x sites to block the HER activity, while this effect is negligible

for Ni NPs. As shown in **Fig. 6b**, the current densities of NC/Ni/TiO_2 NPAs and NWAs are reduced from 38 to 32 mA cm^{-2} and 33 to 29 mA cm^{-2} within 30 s (around 15 % drop) at the applied potentials of -170 and -276 mV, respectively. The current densities of Ni/TiO_2 NPAs and NWAs, however, remain unchanged. The HER activity of NC/Ni/TiO_2 NPAs and NWAs are also evaluated by LSV conducted in 1.0 M KOH electrolyte containing 10 mM KSCN for 2 h (**Fig. S19**). The polarization plots of NC/Ni/TiO_2 NPAs and NWAs show the drop of current densities at -0.2 V by 51 and 55 %, respectively. Such reduced current responses in NC/Ni/TiO_2 NPAs and NWAs suggest that the enhanced HER activities of NC/Ni/TiO_2 NPAs and NWAs stem from the formation of active Ni-N-C bonds at the NC QD/Ni NP interface. This may provide an explanation for the significant HER enhancement observed from the NC/Ni/TiO_2 NWAs where the Ni NPs on inactive TiO_2(110) facets are activated by forming Ni-N-C bonds.

4 Conclusion

In summary, we presented two novel approaches to improve the catalytic activity of Ni NPs by adjusting the morphology of the TiO_2 substrate and modifying nitrogen-doped carbon on the surface of Ni NPs. Compared to Ni/TiO_2 NWAs, Ni/TiO_2 NPAs exhibits a higher HER performance with a low overpotential of 88 mV at 10 mA cm^{-2} and a small Tafel slope of 78 mV dec^{-1}, which is attributed the highly active Ni NPs on the (001) facets of TiO_2 NPAs. The inactive Ni NPs on the {110} facets can be activated by coating the NC QD layer that constructs an active interface between Ni NPs and nitrogen-doped carbon. Such layer of NC QDs also substantially improved the stability of NC/Ni/TiO_2 NPAs. We demonstrated how the intrinsic HER activity of Ni NPs can be optimized, which would provide a guide to the rational design

of low-cost transition metal HER catalysts for high activity.

Acknowledgments

This work was supported by the Innovation and Technology Commission of Hong Kong and Hong Kong Polytechnic University (Grant No: 1-BE0Y), and the Global Frontier Program through the Global Frontier Hybrid Interface Materials (GFHIM) of National Research Foundation of Korea (NRF) funded by the Ministry of Science and ICT (Project No. 2013M3A6B1078882).

Appendix A. Supporting Information

Supplementary data including SEM images, XRD patterns, Raman spectra, XPS results, and electrochemical curves associated with this article can be found in the online version at doi:

Conflict of Interest

The authors declare no conflict of interest.

References

[1] Y. Jiao, Y. Zheng, K. Davey, S.Z. Qiao, Activity origin and catalyst design principles for electrocatalytic hydrogen evolution on heteroatom-doped graphene, Nat. Energy 1 (2016) 1–9. doi:10.1038/nenergy.2016.130.

[2] P.W. Menezes, A. Indra, I. Zaharieva, C. Walter, S. Loos, S. Hoffmann, R. Schlögl, H. Dau, M. Driess, Helical cobalt borophosphates to master durable overall water-splitting, Energy Environ. Sci. 12 (2019) 988–999. doi:10.1039/c8ee01669k.

[3] H. Zhou, F. Yu, J. Sun, R. He, S. Chen, C.W. Chu, Z. Ren, Highly active catalyst derived from a 3D foam of $Fe(PO_3)_2/Ni_2P$ for extremely efficient water oxidation, Proc. Natl. Acad. Sci. U. S. A. 114 (2017) 5607–5611. doi:10.1073/pnas.1701562114.

[4] H. Zhang, X. Li, A. Hähnel, V. Naumann, C. Lin, S. Azimi, S.L. Schweizer, A.W. Maijenburg, R.B. Wehrspohn, Bifunctional heterostructure assembly of NiFe LDH nanosheets on NiCoP nanowires for highly efficient and stable overall water splitting, Adv. Funct. Mater. 28 (2018) 1–10. doi:10.1002/adfm.201706847.

[5] F. Guo, Y. Wu, H. Chen, Y. Liu, L. Yang, X. Ai, X. Zou, High-performance oxygen evolution electrocatalysis by boronized metal sheets with self-functionalized surfaces, Energy Environ. Sci. 12 (2019) 684–692. doi:10.1039/c8ee03405b.

[6] J. Zhang, T. Wang, D. Pohl, B. Rellinghaus, R. Dong, S. Liu, X. Zhuang, X. Feng, Interface engineering of MoS_2/Ni_3S_2 heterostructures for highly enhanced electrochemical overall-water-splitting activity, Angew. Chem. Int. Ed. 55 (2016) 6702–6707. doi:10.1002/anie.201602237.

[7] K. Ojha, S. Saha, P. Dagar, A. K. Ganguli, Nanocatalysts for hydrogen evolution reactions, Phys. Chem. Chem. Phys. 20 (2018) 6777-6799. doi: 10.1039/c7cp06316d.

[8] L. Xie, F. Qu, Z. Liu, X. Ren, S. Hao, R. Ge, G. Du, A. M. Asiri, X. Sun, L. Chen, *In situ* formation of a 3D core/shell structured Ni_3N@Ni-Bi nanosheet array: an efficient non-noble-metal bifunctinal electrocatalyst toward full water splitting under near-neutral conditions, J. Mater. Chem. A 5 (2017) 7806-7810. doi: 10.1039/c7ta02333b.

[9] W. Sheng, M. Myint, J.G. Chen, Y. Yan, Correlating the hydrogen evolution reaction activity in alkaline electrolytes with the hydrogen binding energy on monometallic surfaces, Energy Environ. Sci. 6 (2013) 1509–1512. doi:10.1039/c3ee00045a.

[10] J. Deng, P. Ren, D. Deng, L. Yu, F. Yang, X. Bao, Highly active and durable non-precious-metal hydrogen evolution reaction, Energy Environ. Sci. 7 (2014) 1919–1923. doi:10.1039/c4ee00370e.

[11] C. Dong, X. Liu, X. Wang, X. Yuan, Z. Xu, W. Dong, M.S. Riaz, G. Li, F. Huang, Hierarchical Ni/$NiTiO_3$ derived from NiTi LDHs: a bifunctional electrocatalyst for overall water splitting, J. Mater. Chem. A 15 (2017) 24767–24774. doi:10.1039/c7ta08440d.

[12] Y. An, B. Huang, Z. Wang, X. Long, Y. Qiu, J. Hu, D. Zhou, H. Lin, S. Yang, Constructing three-dimensional porous Ni/Ni_3S_2 nano-interfaces for hydrogen evolution electrocatalysis under alkaline conditions, Dalt. Trans. 46 (2017) 10700–10706. doi:10.1039/c7dt00878c.

[13] J. Feng, H. Xu, Y. Dong, X. Lu, Y. Tong, G. Li, Efficient hydrogen evolution

electrocatalysis using cobalt nanotubes decorated with titanium dioxide nanodots, Angew. Chem. Int. Ed. 56 (2017) 2960–2964. doi:10.1002/anie.201611767.

[14] W. Guo, C. Xu, X. Wang, S. Wang, C. Pan, C. Lin, Z.L. Wang, Rectangular bunched rutile TiO_2 nanorod arrays grown on carbon fiber for dye-sensitized solar cells, J. Am. Chem. Soc. 134 (2012) 4437–4441. doi:10.1021/ja2120585.

[15] W. Guo, F. Zhang, C. Lin, Z.L. Wang, Direct growth of TiO_2 nanosheet arrays on carbon fibers for highly efficient photocatalytic degradation of methyl orange, Adv. Mater. 24 (2012) 4761–4764. doi:10.1002/adma.201201075.

[16] Y. Dong, S.Y. Chen, Y. Lu, Y.X. Xiao, J. Hu, S.M. Wu, Z. Deng, G. Tian, G.G. Chang, J. Li, S. Lenaerts, C. Janiak, X.Y. Yang, B.L. Su, Hierarchical MoS_2@TiO_2 heterojunctions for enhanced photocatalytic performance and electrocatalytic hydrogen evolution, Chem. - An Asian J. 13 (2018) 1609–1615. doi:10.1002/asia.201800359.

[17] K. Wang, Q. Chen, Y. Hu, W. Wei, S. Wang, Q. Shen, P. Qu, Crystalline $Ru_{0.33}Se$ nanoparticles-decorated TiO_2 nanotube arrays for enhanced hydrogen evolution reaction, Small 14 (2018) 1–9. doi:10.1002/smll.201802132.

[18] H. Sun, W. Lu, J. Zhao, Structure and reactivity of anatase TiO_2(001)-(1 × 4) surface, J. Phys. Chem. C 122 (2018) 14528–14536. doi:10.1021/acs.jpcc.8b02777.

[19] A. Fujishima, X. Zhang, D.A. Tryk, TiO_2 photocatalysis and related surface phenomena, Surf. Sci. Rep. 63 (2008) 515–582. doi:10.1016/j.surfrep.2008.10.001.

[20] H.G. Yang, C.H. Sun, S.Z. Qiao, J. Zou, G. Liu, S.C. Smith, H.M. Cheng, G.Q. Lu, Anatase TiO_2 single crystals with a large percentage of reactive facets, Nature 453 (2008)

638–641. doi:10.1038/nature06964.

[21] F. Izumi, The polymorphic crystallization of titanium(IV) oxide under hydro-thermal conditions. II. the roles of inorganic anions in the nucleation of rutile and anatase from acid solutions, Bull. Chem. Soc. Jpn. 51 (1978) 1771–1776. doi:10.1246/bcsj.51.1771.

[22] M. Zhu, Y. Zhou, Y. Sun, C. Zhu, L. Hu, J. Gao, H. Huang, Y. Liu, Z. Kang, Cobalt phosphide/carbon dots composite as an efficient electrocatalyst for oxygen evolution reaction, Dalt. Trans. 47 (2018) 5459–5464. doi:10.1039/c7dt04291d.

[23] T. Bao, L. Song, S. Zhang, Synthesis of carbon quantum dot-doped NiCoP and enhanced electrocatalytic hydrogen evolution ability and mechanism, Chem. Eng. J. 351 (2018) 189–194. doi:10.1016/j.cej.2018.06.080.

[24] W. Li, Y. Liu, M. Wu, X. Feng, S.A.T. Redfern, Y. Shang, X. Yong, T. Feng, K. Wu, Z. Liu, B. Li, Z. Chen, J.S. Tse, S. Lu, B. Yang, Carbon-quantum-dots-loaded ruthenium nanoparticles as an efficient electrocatalyst for hydrogen production in alkaline media, Adv. Mater. 30 (2018) 1–8. doi:10.1002/adma.201800676.

[25] Y. Yang, J. Liu, S. Guo, Y. Liu, Z. Kang, A nickel nanoparticle/carbon quantum dot hybrid as an efficient electrocatalyst for hydrogen evolution under alkaline conditions, J. Mater. Chem. A 3 (2015) 18598–18604. doi:10.1039/c5ta04867b.

[26] Y. Liu, X. Li, Q. Zhang, W. Li, Y. Xie, H. Liu, L. Shang, Z. Liu, Z. Chen, L. Gu, Z. Tang, T. Zhang, S. Lu, A general route to prepare low-ruthenium-content bimetallic electrocatalysts for pH-universal hydrogen evolution reaction by using carbon quantum dots, Angew. Chem. Int. Ed. 59 (2020) 1718-1726. doi.org/10.1002/anie.201913910.

[27] Y. Liu, Y. Yang, Z. Peng, Z. Liu, Z. Chen, L. Shang, S. Lu, T. Zhang, Self-crosslinking carbon dots loaded ruthenium dots as an efficient and super-stable hydrogen production electrocatalyst at all pH values, Nano Energy 65 (2019) 104023. doi.org/10.1016/j.nanoen.2019.104023.

[28] J. Deng, P. Ren, D. Deng, X. Bao, Enhanced electron penetration through an ultrathin graphene layer for highly efficient catalysis of the hydrogen evolution reaction, Angew. Chem. Int. Ed. 54 (2015) 2100–2104. doi:10.1002/anie.201409524.

[29] W. Zhou, J. Zhou, Y. Zhou, J. Lu, K. Zhou, L. Yang, Z. Tang, L. Li, S. Chen, N-doped carbon-wrapped cobalt nanoparticles on N-doped graphene nanosheets for high-efficiency hydrogen production, Chem. Mater. 27 (2015) 2026–2032. doi:10.1021/acs.chemmater.5b00331.

[30] W. Zhou, J. Jia, J. Lu, L. Yang, D. Hou, G. Li, S. Chen, Recent developments of carbon-based electrocatalysts for hydrogen evolution reaction, Nano Energy 28 (2016) 29–43. doi:10.1016/j.nanoen.2016.08.027.

[31] Y.Q. Zhang, D.K. Ma, Y.G. Zhang, W. Chen, S.M. Huang, N-doped carbon quantum dots for TiO_2-based photocatalysts and dye-sensitized solar cells, Nano Energy 2 (2013) 545–552. doi:10.1016/j.nanoen.2013.07.010.

[32] R. Shi, Z. Li, H. Yu, L. Shang, C. Zhou, G.I.N. Waterhouse, L.Z. Wu, T. Zhang, Effect of nitrogen doping level on the performance of N-doped carbon quantum dot/TiO_2 composites for photocatalytic hydrogen evolution, ChemSusChem 10 (2017) 4650–4656. doi:10.1002/cssc.201700943.

[33] Z. Qian, J. Ma, X. Shan, H. Feng, L. Shao, J. Chen, Highly luminescent N-doped carbon quantum dots as an effective multifunctional fluorescence sensing platform, Chem. - Eur. J. 20 (2014) 2254–2263. doi:10.1002/chem.201304374.

[34] J.P. Perdew, K. Burke, M. Ernzerhof, Generalized gradient approximation made simple, Phys. Rev. Lett. 77 (1996) 3865–3868. doi:10.1103/PhysRevLett.77.3865.

[35] W. Kohn, L.J. Shan, Self-consistent equations including exchange and correlation effects, Phys. Rev. 140 (1965) A1133–A1138. https://doi.org/10.1103/PhysRev.140.A1133.

[36] G. Kresse, J. Furthmüller, Efficiency of ab-initio total energy calculations for metals and semiconductors using a plane-wave basis set, Comput. Mater. Sci. 6 (1996) 15–50. doi:10.1016/0927-0256(96)00008-0.

[37] G. Kresse, J. Furthmüller, Efficient iterative schemes for ab initio total-energy calculations using a plane-wave basis set, Phys. Rev. B 54 (1996) 11169–11186. doi:10.1103/PhysRevB.54.11169.

[38] P.E. Blöchl, Projector augmented-wave method, Phys. Rev. B 50 (1994) 17953–17979. doi:10.1103/PhysRevB.50.17953.

[39] S. Grimme, J. Antony, S. Ehrlich, H. Krieg, A consistent and accurate ab initio parametrization of density functional dispersion correction (DFT-D) for the 94 elements H-Pu, J. Chem. Phys. 132 (2010) 154104. doi:10.1063/1.3382344.

[40] H. Cheng, J. Ma, Z. Zhao, L. Qi, Hydrothermal preparation of uniform nanosize rutile and anatase particles, Chem. Mater. 7 (1995) 663–671. doi:10.1021/cm00052a010.

[41] A. Kumar, A.R. Madaria, C. Zhou, Growth of aligned single-crystalline rutile TiO_2 nanowires on arbitrary substrates and their application in dye-sensitized solar cells, J. Phys. Chem. C 114 (2010) 7787–7792. doi:10.1021/jp100491h.

[42] Y.S. Hu, L. Kienle, Y.G. Guo, J. Maier, High lithium electroactivity of nanometer-sized rutile TiO_2, Adv. Mater. 18 (2006) 1421–1426. doi:10.1002/adma.200502723.

[43] L.G. Devi, N. Kottam, B.N. Murthy, S.G. Kumar, Enhanced photocatalytic activity of transition metal ions Mn^{2+}, Ni^{2+} and Zn^{2+} doped polycrystalline titania for the degradation of Aniline Blue under UV/solar light, J. Mol. Catal. A Chem. 328 (2010) 44–52. doi:10.1016/j.molcata.2010.05.021.

[44] M. Kim, J. Seo, D. Zhao, S. Liu, K. Kim, K. Lim, W. Zhou, E. Waks, Z. Ma, Correction : Transferrable single crystalline, J. Mater. Chem. C 5 (2017) 264–268. doi:10.1039/c7tc90009k.

[45] H. Liang, A.N. Gandi, C. Xia, M.N. Hedhili, D.H. Anjum, U. Schwingenschlögl, H.N. Alshareef, Amorphous NiFe-OH/NiFeP electrocatalyst fabricated at low temperature for water oxidation applications, ACS Energy Lett. 2 (2017) 1035–1042. doi:10.1021/acsenergylett.7b00206.

[46] L. Yu, S. Yu, D. Li, Direct combination of hydrogen evolution from water and methane conversion in a photocatalytic system over Pt/TiO_2, Appl. Catal. B Environ. 5 (2017) 216–223. doi:10.1016/j.apcatb.2016.11.039.

[47] P. Chen, K. Xu, Z. Fang, Y. Tong, J. Wu, X. Lu, X. Peng, H. Ding, C. Wu, Y. Xie, Metallic Co_4N porous nanowire arrays activated by surface oxidation as electrocatalysts

for the oxygen evolution reaction, Angew. Chem. Int. Ed. 54 (2015) 14710–14714. doi:10.1002/anie.201506480.

[48] A.J. Medford, A. Vojvodic, J.S. Hummelshøj, J. Voss, F. Abild-Pedersen, F. Studt, T. Bligaard, A. Nilsson, J.K. Nørskov, From the Sabatier principle to a predictive theory of transition-metal heterogeneous catalysis, J. Catal. 328 (2015) 36–42. doi:10.1016/j.jcat.2014.12.033.

[49] J. Gu, W. Wang, Q. Zhang, Z. Meng, X. Jia, K. Xi, Synthesis of fluorescent carbon nanoparticles from polyacrylamide for fast cellular endocytosis, RSC Adv. 3 (2013) 15589–15591. doi:10.1039/c3ra41654b.

[50] H. Ji, F. Zhou, J. Gu, C. Shu, K. Xi, X. Jia, Nitrogen-doped carbon dots as a new substrate for sensitive glucose determination, Sensors 16 (2016) 1–10. doi:10.3390/s16050630.

[51] Z. Qiu, C.W. Tai, G.A. Niklasson, T. Edvinsson, Direct observation of active catalyst surface phases and the effect of dynamic self-optimization in NiFe-layered double hydroxides for alkaline water splitting, Energy Environ. Sci. 12 (2019) 572–581. doi:10.1039/c8ee03282c.

[52] C. Lei, Y. Wang, Y. Hou, P. Liu, J. Yang, T. Zhang, X. Zhuang, M. Chen, B. Yang, L. Lei, C. Yuan, M. Qiu, X. Feng, Efficient alkaline hydrogen evolution on atomically dispersed Ni-N_x Species anchored porous carbon with embedded Ni nanoparticles by accelerating water dissociation kinetics, Energy Environ. Sci. 12 (2019) 149–156. doi:10.1039/c8ee01841c.

Figure Captions

Fig. 1. (a) Schematics of synthetic procedure for TiO_2 NWAs and NPAs. (b) SEM, (c) TEM, and (d) HRTEM images of TiO_2 NWAs. The inset in (b) is a cross-sectional SEM image. (e) SEM, (f) TEM, and (g and h) HRTEM images of TiO_2 NPAs. The insets in (e) are the cross-sectional (top-right) and side-view (bottom-left) SEM images. (i) The corresponding SAED pattern of TiO_2 NPAs.

Fig. 2. SEM images of (a) Ni/TiO_2 NWAs and (b) Ni/TiO_2 NPAs. Insets in (a) and (b) are the corresponding TEM images of single nanowire and nanopyramid, respectively. HRTEM images of (c) Ni/TiO_2 NWAs and (d) Ni/TiO_2 NPAs. (e) XRD patterns of Ni/TiO_2 NPAs, e-TiO_2 NPAs, Ni/TiO_2 NWAs, and e-TiO_2 NWAs. (f) Mass loading of Ni NPs in Ni/TiO_2 NPAs and NWAs and the doped Ni in e-TiO_2 NPAs and NWAs.

Fig. 3. XPS spectra of Ni/TiO_2 NPAs, e-TiO_2 NPAs, Ni/TiO_2 NWAs, and e-TiO_2 NWAs in (a) Ni $2p_{3/2}$ and (b) O 1s regions. Plane-averaged charge density differences (Δn) of (c) Ni/TiO_2(110) and (d) Ni/TiO_2(001).

Fig. 4. (a) Polarization curves and (b) Tafel plots of Ni/TiO_2 NPAs, Ni/TiO_2 NWAs, e-TiO_2 NPAs, e-TiO_2 NWAs, carbon cloth, and Pt/C. (c) Amperometric test of Ni/TiO_2 NPAs at an applied potential of -0.126 V for 17 h. (d) Comparison of C_{dl} of Ni/TiO_2 NPAs, Ni/TiO_2 NWAs,

e-TiO_2 NPAs, and e-TiO_2 NWAs. (e) TOF plots of Ni/TiO_2 NPAs and NWAs. (f) Free-energy diagram for H adsorption on the Ni/TiO_2(001) and (110) surfaces.

Fig. 5. (a) Polarization curves and (b) Tafel plots of NC/Ni/TiO_2 NPAs, Ni/TiO_2 NPAs, NC/Ni/TiO_2 NWAs, Ni/TiO_2 NWAs, and Pt/C. Comparisons of the overpotentials at 10 mA cm^{-2} for (c) NC/Ni/TiO_2 and Ni/TiO_2 NPAs and (d) NC/Ni/TiO_2 and Ni/TiO_2 NWAs. (e) Amperometric test of NC/Ni/TiO_2 NPAs at two applied overpotentials (-226 and -326 mV) for 15 h each.

Fig. 6. (a) *In situ* Raman spectroscopy of NC/Ni/TiO_2 NPAs in a range of potentials from -0.024 to -0.424 V with an interval of 50 mV. (b) Amperometric *i*-t test of NC/Ni/TiO_2 NPAs, Ni/TiO_2 NPAs, NC/Ni/TiO_2 NWAs, and Ni/TiO_2 NWAs at applied potentials of -170, -276, -276, and -476 mV, respectively, with the current response to the injection of 5 mM KSCN indicated by arrows.

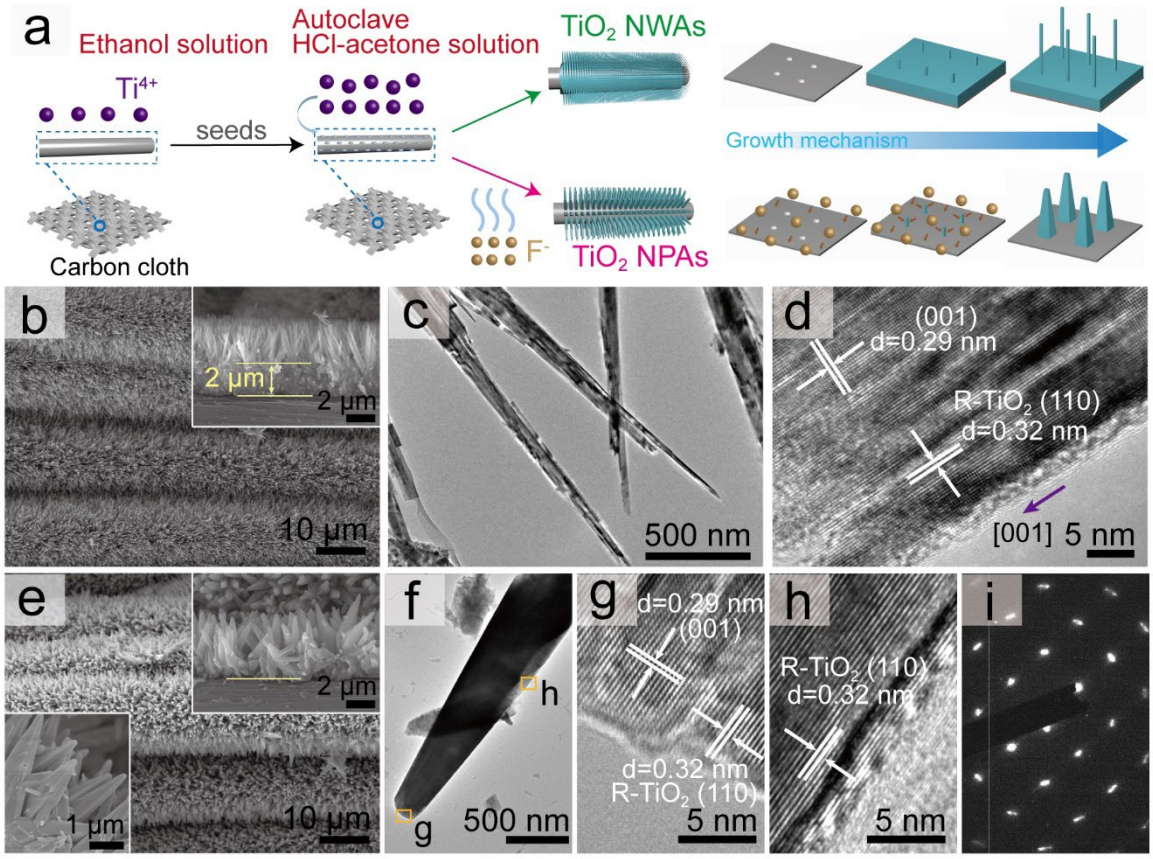
a
Ethanol solution
Autoclave
HCl-acetone solution
TiO2 NWAs
Ti4+
seeds
Carbon cloth
F-
TiO2 NPAs
Growth mechanism
b
2 μm
2 μm
10 μm
c
500 nm
d
(001)
d=0.29 nm
R-TiO2 (110)
d=0.32 nm
[001] 5 nm
e
2 μm
1 μm
10 μm
f
h
g
500 nm
g
d=0.29 nm
(001)
d=0.32 nm
R-TiO2 (110)
5 nm
h
R-TiO2 (110)
d=0.32 nm
5 nm
i

Figure 1

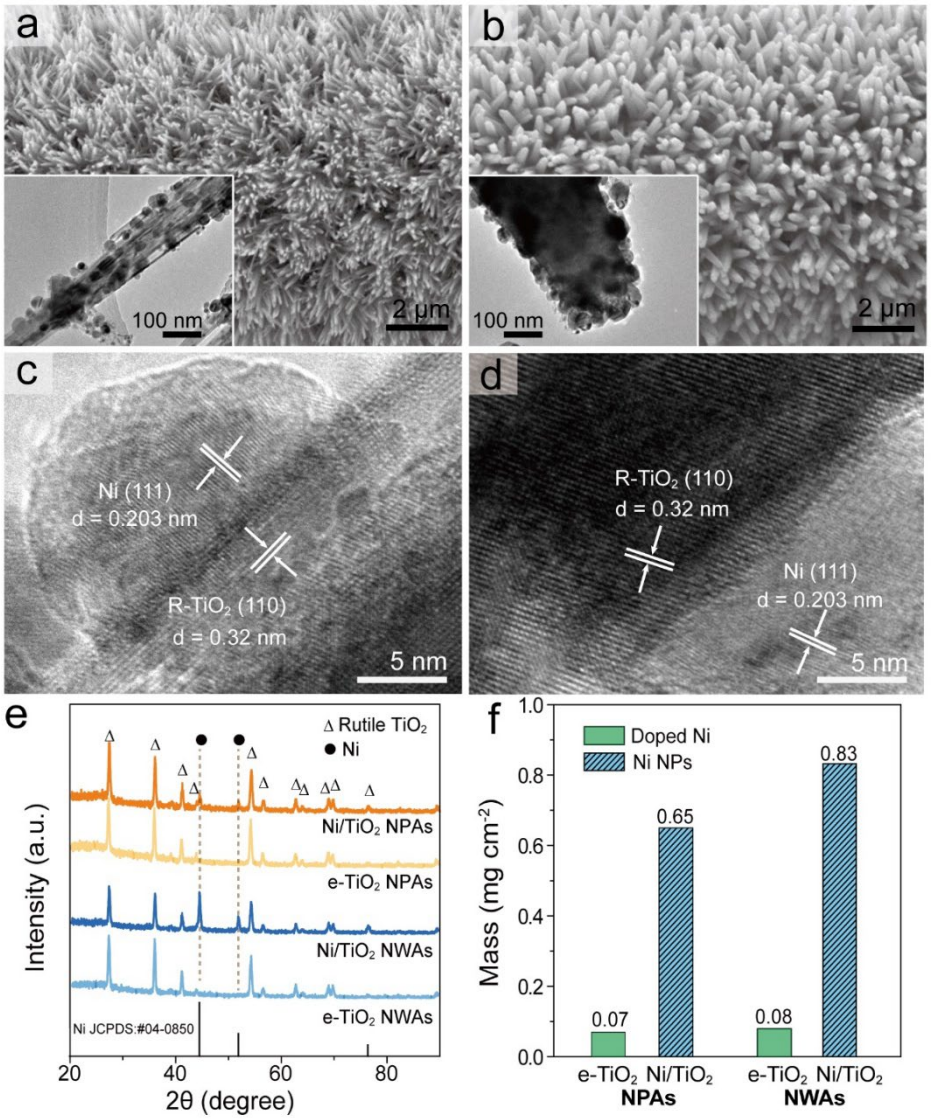
a
100 nm
2 μm
b
100 nm
2 μm
c
Ni (111)
d = 0.203 nm
R-TiO2 (110)
d = 0.32 nm
5 nm
d
R-TiO2 (110)
d = 0.32 nm
Ni (111)
d = 0.203 nm
5 nm
e
Δ Rutile TiO2
● Ni
Ni/TiO2 NPAs
e-TiO2 NPAs
Ni/TiO2 NWAs
e-TiO2 NWAs
Ni JCPDS:#04-0850
Intensity (a.u.)
20
40
60
80
2θ (degree)
f
Doped Ni
Ni NPs
Mass (mg cm-2)
0.0
0.2
0.4
0.6
0.8
1.0
0.07
0.65
0.08
0.83
e-TiO2 Ni/TiO2
NPAs
e-TiO2 Ni/TiO2
NWAs

Figure 2

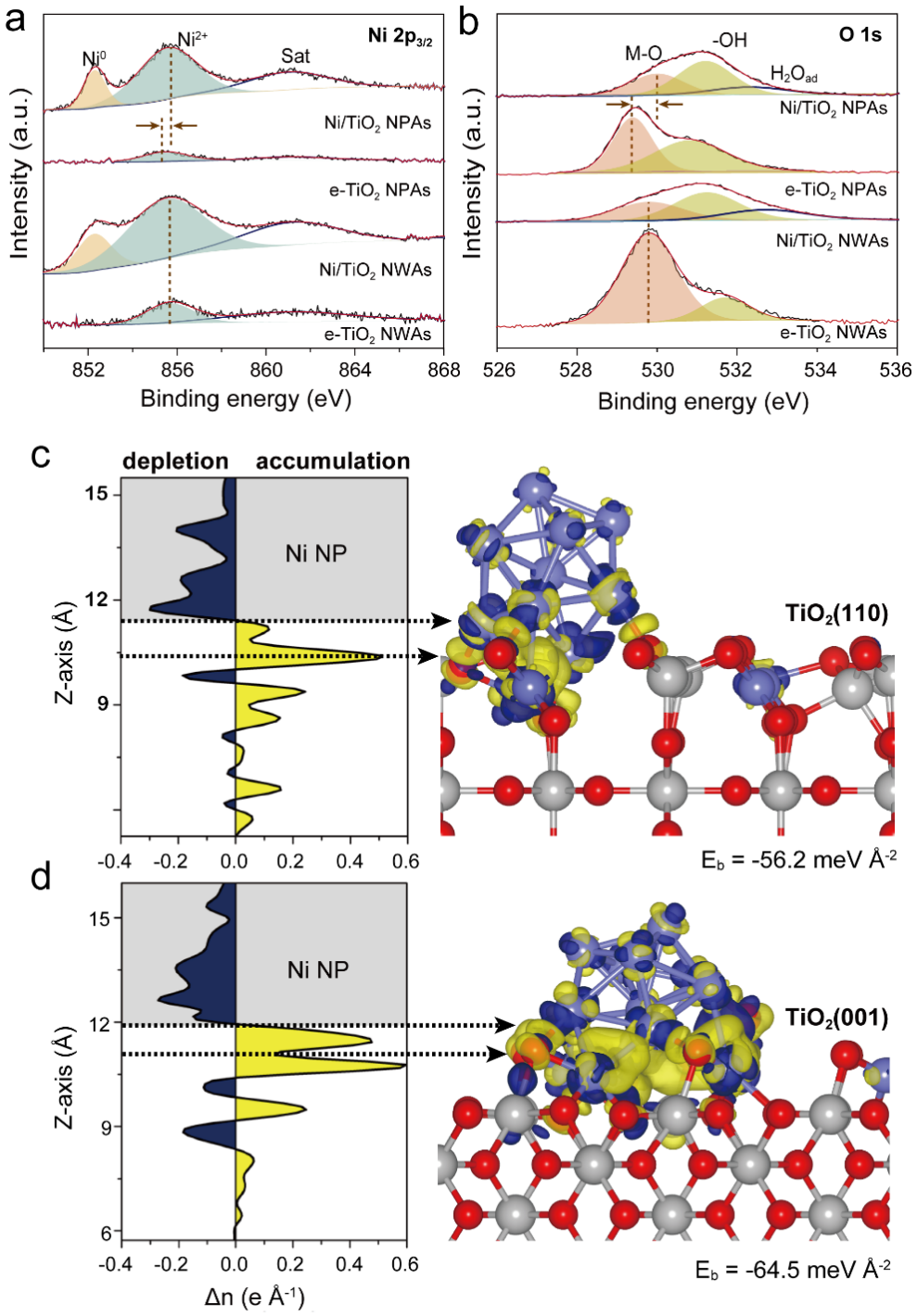
a
Ni 2p3/2
Ni0
Ni2+
Sat
Ni/TiO2 NPAs
e-TiO2 NPAs
Ni/TiO2 NWAs
e-TiO2 NWAs
Intensity (a.u.)
852
856
860
864
868
Binding energy (eV)
b
O 1s
M-O
-OH
H2Oad
Ni/TiO2 NPAs
e-TiO2 NPAs
Ni/TiO2 NWAs
e-TiO2 NWAs
Intensity (a.u.)
526
528
530
532
534
536
Binding energy (eV)
c
depletion
accumulation
Ni NP
Z-axis (Å)
15
12
9
-0.4
-0.2
0.0
0.2
0.4
0.6
TiO2(110)
Eb = -56.2 meV Å-2
d
Ni NP
Z-axis (Å)
15
12
9
6
-0.4
-0.2
0.0
0.2
0.4
0.6
Δn (e Å-1)
TiO2(001)
Eb = -64.5 meV Å-2

Figure 3

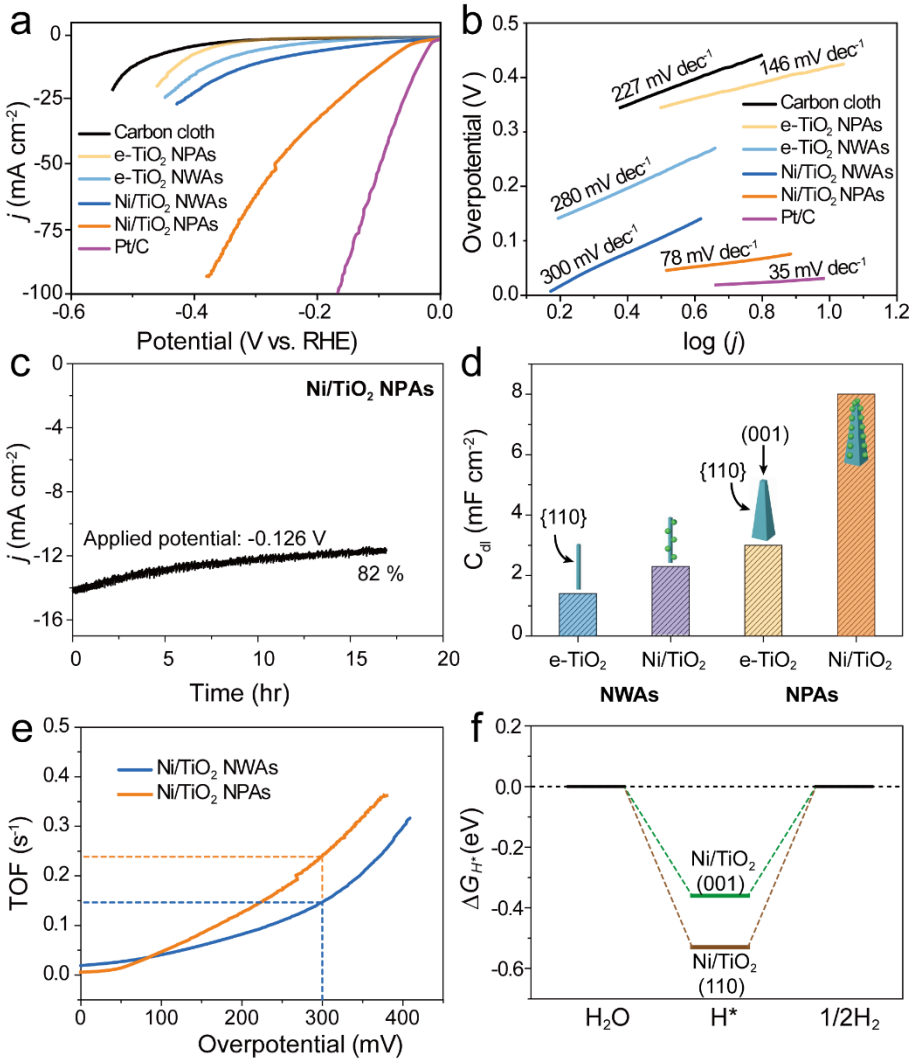
a
j (mA cm-2)
Potential (V vs. RHE)
Carbon cloth
e-TiO2 NPAs
e-TiO2 NWAs
Ni/TiO2 NWAs
Ni/TiO2 NPAs
Pt/C
b
Overpotential (V)
log (j)
227 mV dec-1
146 mV dec-1
280 mV dec-1
300 mV dec-1
78 mV dec-1
35 mV dec-1
c
Ni/TiO2 NPAs
Applied potential: -0.126 V
82 %
Time (hr)
d
Cdl (mF cm-2)
{110}
(001)
e-TiO2
Ni/TiO2
NWAs
NPAs
e
TOF (s-1)
Overpotential (mV)
f
ΔGH* (eV)
Ni/TiO2 (001)
Ni/TiO2 (110)
H2O
H*
1/2H2

Figure 4

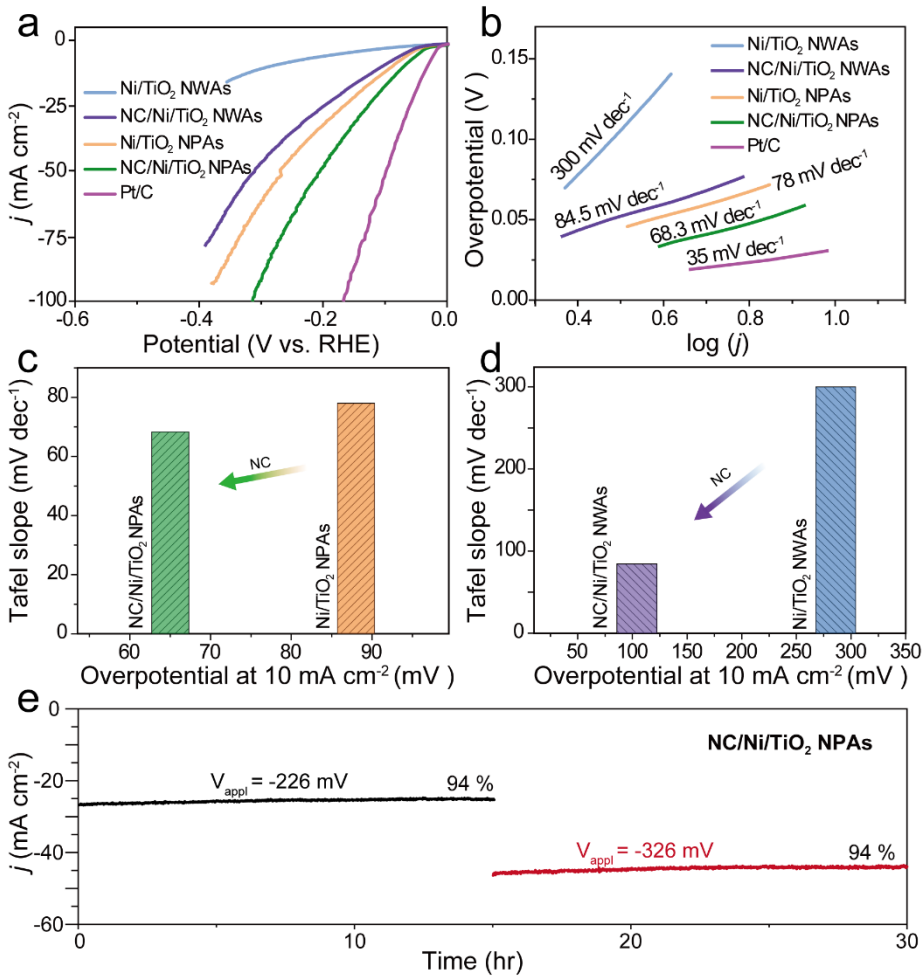
a
b
c
d
e
Ni/TiO2 NWAs
NC/Ni/TiO2 NWAs
Ni/TiO2 NPAs
NC/Ni/TiO2 NPAs
Pt/C
j (mA cm-2)
Potential (V vs. RHE)
Overpotential (V)
log (j)
300 mV dec-1
84.5 mV dec-1
78 mV dec-1
68.3 mV dec-1
35 mV dec-1
Tafel slope (mV dec-1)
NC
Overpotential at 10 mA cm-2 (mV)
NC/Ni/TiO2 NPAs
Ni/TiO2 NPAs
NC/Ni/TiO2 NWAs
Ni/TiO2 NWAs
NC/Ni/TiO2 NPAs
Vappl = -226 mV
94 %
Vappl = -326 mV
94 %
Time (hr)

Figure 5

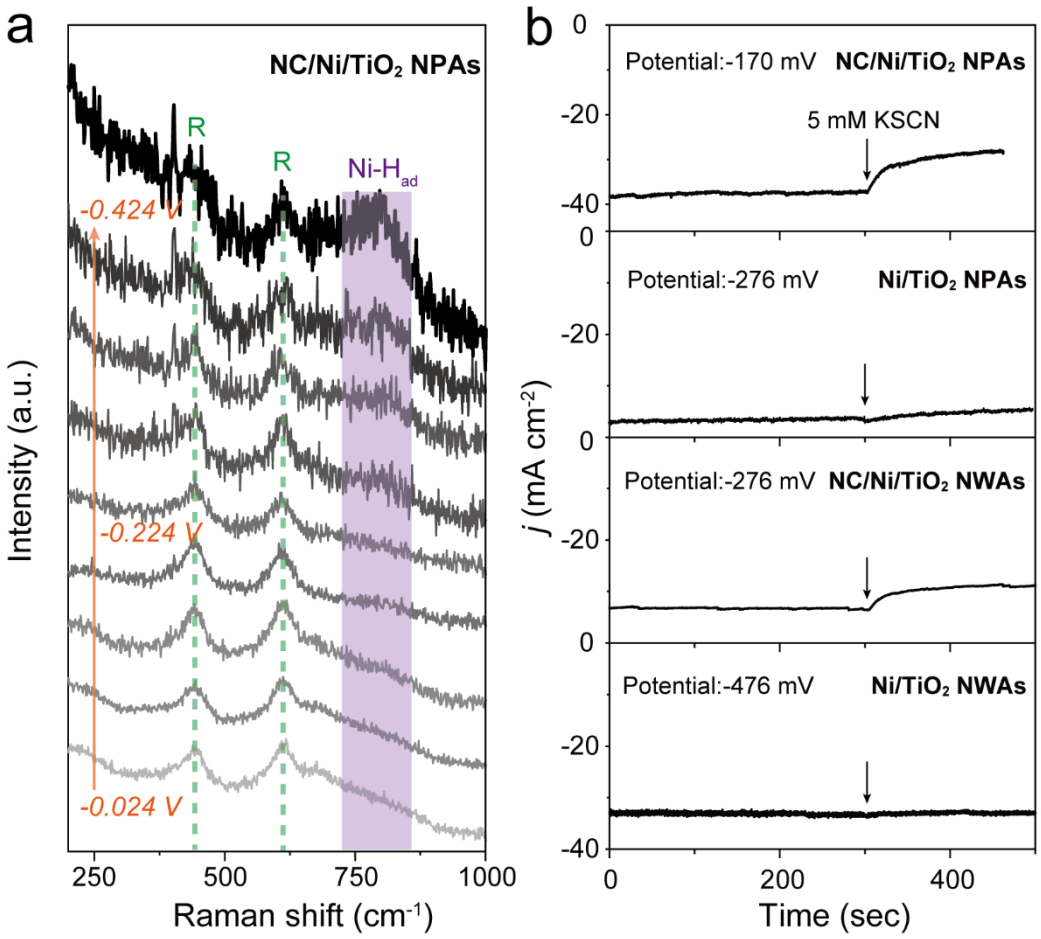
a
NC/Ni/TiO2 NPAs
R
R
Ni-Had
-0.424 V
-0.224 V
-0.024 V
Intensity (a.u.)
250
500
750
1000
Raman shift (cm-1)
b
Potential:-170 mV NC/Ni/TiO2 NPAs
5 mM KSCN
Potential:-276 mV Ni/TiO2 NPAs
Potential:-276 mV NC/Ni/TiO2 NWAs
Potential:-476 mV Ni/TiO2 NWAs
j (mA cm-2)
0
-20
-40
0
200
400
Time (sec)

Figure 6